Available online at www.sciencedirect.com
ScienceDirect
Acta Materialia xxx (2008) xxx–xxx
Acta MATERIALIA
www.elsevier.com/locate/actamat

Influence of ceramic–metal interface adhesion on crack growth resistance of 3Y-TZP–Nb ceramic matrix composites

J.F. Bartolomé, J.I. Beltrán, C.F. Gutiérrez-González, C. Pecharromán, M.C. Muñoz, J.S. Moya *

Instituto de Ciencia de Materiales de Madrid, Consejo Superior de Investigaciones Científicas (CSIC), C/Sor Juana Inés de la Cruz 3, 28049 Madrid, Spain

Received 22 December 2007; received in revised form 11 March 2008; accepted 12 March 2008

Abstract

Yttria-stabilized zirconia strengthened with lamellar flaky-shape Nb metal particles was obtained by hot-pressing at 1500 °C for 1 h. The ZrO_2–Nb interface has been studied by atomistic, first-principles calculations and by high-resolution transmission electron microscopy. The influence of the ceramic–metal interface on the crack growth resistance has been investigated. Crack growth is shown to occur with a rising resistance, governed by intact metal ligaments in the crack wake. Crack extension occurs by a combination of plastic deformation on the metal particles and interface debonding. The connection between the interface adhesion and this microstructural toughening mechanism has been evaluated.

Keywords: Toughness; Cermets; Interface structure; HRTEM; Abhishiktananda initio electron theory

1. Introduction

It has been widely recognized that the major limitation of ceramics for structural applications is their low fracture toughness. Brittle ceramics can be toughened by introducing a ductile phase into them. The concept of ductile phase toughening of brittle materials is not new. It was proposed originally by Krstic [1] as a means of increasing the energy dissipation (by plastic stretching of ductile phase) in brittle materials. Since this pioneering work, there have been considerable efforts to improve the fracture toughness of brittle materials by the incorporation of ductile phases [2–7]. The structural configurations of interfacial boundaries as well as the chemical bonding state between the reinforcement component and the monolithic baseline material define a fundamental issue of ceramic–metal composite research. However, the influence of its nature on the crack growth behavior of ductile phase-toughened composites has been little explored. The main problem is that the bridging stresses of the metal ligaments cannot be measured directly in an experiment, although it is an important material-specific property which substantially controls the mechanical performance of the composite. This stress relation is dependent mainly on the properties of the metal–ceramic interface. Adhesion and debonding strongly affect energy dissipation during fracture of ductile toughened ceramic matrices [8]. If the metal–ceramic bond is very strong, only a relatively small volume of the metal inclusions will be deformed plastically, sometimes accompanied by matrix fracture, giving limited energy dissipation. Conversely, very low bonded interfaces also result in low energy dissipation by crack deflection. Moderate debonding, however, can offer substantial energy dissipation. The mechanisms that contribute to toughening in this particular case are crack bridging by ductile ligaments and crack shielding [9–12]. Our current understanding of the effects of interfacial interactions is not completely described by the available general models, making difficult or almost impossible the design of composites with the desired combinations of fracture

* Corresponding author. Tel.: +34 913 349 083; fax: +34 913 720 623.
E-mail address: jsmoya@icmm.csic.es (J.S. Moya).

1359-6454/$34.00 © 2008 Acta Materialia Inc. Published by Elsevier Ltd. All rights reserved.
doi:10.1016/j.actamat.2008.03.021

toughness, damage tolerance and fatigue resistance. Numerous experimental and theoretical approaches involving high-resolution transmission electron microscopy (HRTEM) studies of metal–ceramic layered systems, bicrystals and epitaxial growth of thin films as well as simulation of grain and phase boundaries have provided quantitative bonding and geometrical models which contribute to a deeper understanding of internal interfaces in composites [13–16]. However, the determination of the local chemistry and structural states across the interfacial boundary of the metal oxide is a challenging task due to its inherent complexity. Moreover, even real interfaces are macroscopic objects; their properties are determined by the atomic structure of the junction. The detailed structure of the interface at the atomistic level is intimately related to the interface electronic properties which in turn control the adhesion properties [17–19]. Therefore, an understanding of these interfaces requires ab initio methods at the atomistic level, connected quantitatively to experimental measurements. Recent ab initio calculations allow to identify the metal adhesion mechanism in certain ceramic–metal interfaces, i.e. solid-state bonding of layered structures, cermets by reduction of laser-assisted directionally solidified lamellar eutectic, nanocomposites or films with epitaxial growth [20–26], suggesting that theoretical methods are useful tools to propose interfaces with optimum adhesion. These rather promising calculations should not give the impression that bonding at an arbitrary ceramic–metal interface could be evaluated by performing ab initio calculations. In previous work [27] we have obtained a ZrO_2–Nb composite with lamellar flaky-shape metal particles with high aspect ratio. This special morphology of the Nb particles promotes a preferential interfacial orientation relationship parallel to the plane of elongated metal grains. In this context, the purpose of this work is the study of adhesion of ZrO_2–Nb ceramic–metal interfaces of bulk composites, using ab initio theoretical calculations. Moreover, we have used the hot-press sintering method in order to ensure that all the lamellar Nb particulates will be textured normal to the crack propagation. The interaction of interfacial characteristics of dissimilar grains with the toughening mechanisms and the mechanical response of ZrO_2–Nb composites are discussed. While the use of K_c as a single-value measure of the toughness is appropriate for many materials, in the ceramic–metal composites the fracture resistance increases with crack extension, promoting stable growth and requiring a resistance curve (R-curve) fracture-mechanics approach [2,28,29]. Different ways have been proposed in the literature to calculate the bridging stress from R-curves measurements [30–32] which can be regarded as some kind of indirect measurement. Therefore, in order to estimate which interfaces are the most likely to exhibit mechanical properties enhancement by plastic deformation, we will discuss the results in terms of crack growth resistance. To the best of our knowledge, this particular ceramic–metal interfacial system has not been previously investigated in the literature.

2. Experimental procedure

2.1. Starting materials

The following commercially available powders have been used as raw materials: (1) Tetragonal zirconia polycrystals (3Y-TZP, 3 mol% Y_2O_3; TZ-3YE, Tosoh Corp.), with an average particle size of $d_{50} = 0.26 \pm 0.05$ μm, a BET specific surface area of 15.4 $m^2\,g^{-1}$ and the following chemical analysis (wt.%): ZrO_2 (94.65), Y_2O_3 (5.07), Al_2O_3 (0.253), SiO_2 (0.005), Na_2O (0.022), Fe_2O_3 (<0.002). (2) Niobium (Goodfellow, 99.85% purity) with an average particle size $d_{50} = 35$ μm.

Niobium powder was attrition-milled with zirconia balls in a teflon container for 4 h using isopropilic alcohol as liquid media. The ball-milled resulting powder consists of flake-like deformed Nb particles with a high aspect ratio and a mean particle size of 41 μm (Fig. 1A). The powder was analyzed by X-ray diffraction (XRD). The specimens for the XRD measurements were prepared by suspending a small volume of Nb powder in acetone directly on a

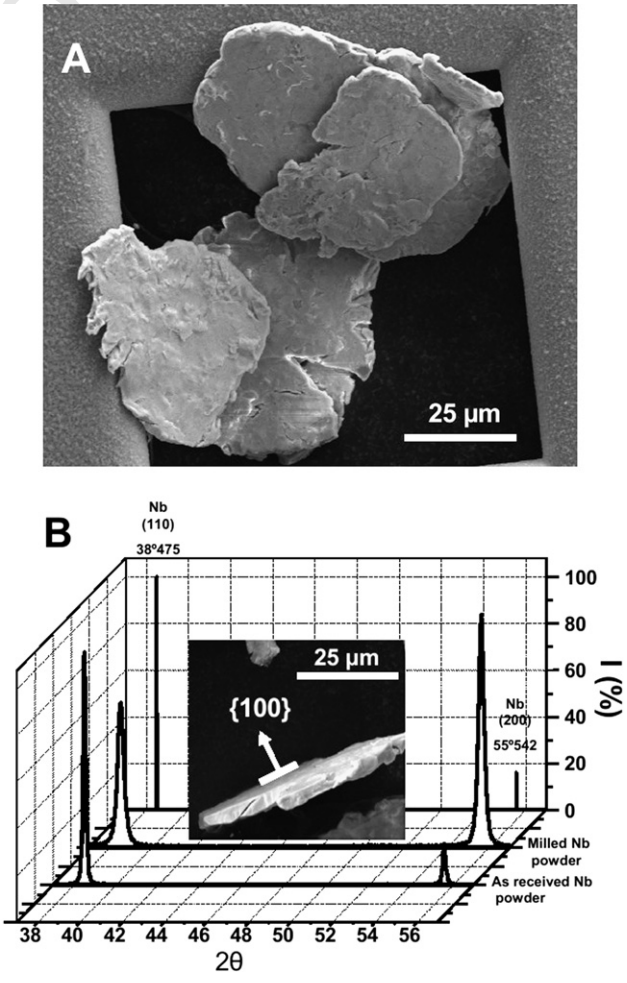

Fig. 1. (A) SEM micrograph of niobium powder after wet ball-milling for 4 h. (B) The 200 and 110 reflections of Nb for an as-received and milled powder. Upon ball-milling, pronounced texturing and broadening occurs as a result of deformation and the increase of lattice strain.

Please cite this article in press as: Bartolomé JF et al., Influence of ceramic–metal interface adhesion on crack ..., Acta Mater (2008), doi:10.1016/j.actamat.2008.03.021

Si(5 1 0) single-crystal wafer within a specially made supporting assembly and drying the suspension by evaporating the acetone. An evenly spread distribution on Nb powder was observed. The X-ray diffraction powder patterns were collected in a Philips Xpert diffractometer operated in the Bragg–von Brentano configuration, which was fitted with an incident-beam Ge(1 1 1) monochromator of the Johansson symmetric type, aligned to select the Cu Kα1 emission, $\lambda = 1.5405981$ Å. During the measurement the specimen was spinning around an axis perpendicular to its surface.

2.2. Powder processing

Zirconia–milled niobium suspension of 80 wt.% solid content was prepared using distilled water as liquid media and a 3 wt.% addition of an alkali-free organic polyelectrolyte as surfactant. The relative proportion of Nb was 20 vol.%. The mixture was homogenized by milling with zirconia balls in polyethylene containers at 150 rpm for 24 h and then dried at 90 °C for 12 h. The resulting powders were ground in an agate mortar and subsequently passed through a 75 μm sieve. The powders were consolidated into composite specimens by hot-pressing. The hot-pressing temperature was 1400 °C for 1 h with heating and cooling rates of 600 °C h^{-1} in an inert 100% Ar atmosphere. On reaching the hot-pressing temperature, a uniaxial pressure of 45 MPa was applied. Both pressure and temperature were held for 1 h. As result, disks with 50 mm diameter and 5 mm thickness were obtained.

2.3. Microstructural and mechanical characterization

The microstructure of fired specimens was studied on surfaces polished down to 1 μm by optical microscopy (Leica, DMR model), scanning electron microscopy (SEM, Hitachi, model S3000N) and transmission electron microscopy (TEM-JEOL 4000-EX). The TEM samples were prepared by diamond cutting and mechanical polishing to a thickness of 100 μm, followed by dimpling to a thickness of 20 μm and ion milling at 6.0 keV and 0.5 mA.

With respect to the mechanical properties, *R*-curves were measured to evaluate the resistance to fracture in terms of the stress intensity, K_I, as a function of crack extension, via the indentation-strength method developed by Braun et al. [33]. This method considers a radial crack produced by indentation subjected to the action of a tensile stress due to the monotonically increasing applied stress load during three-point bending. The bending strength was determined using prismatic bars cut from the pieces fired before with 4 mm width, 45 mm length and 3 mm thickness. The tensile surface was polished down to 1 μm. Young's modulus was obtained from the slopes of load–deflection curves. A static extensometer was used to measure the deflection with an error in the measurement of ≈0.1%. Indentation-strength method was performed using bars in which the centers of the tensile faces were indented with a Vickers diamond indenter (leco 100-A, St Joseph, MI) at contact loads between 10 and 500 N. The tests were performed at room temperature using a universal testing machine (Instron Model 4411, Boston, MA) and were conducted in loading direction perpendicular to the lamellar flaky-shape Nb particles. The specimens were loaded to failure with a cross-head speed of 0.5 mm min^{-1} and a span of 40 mm. The hardness was estimated by the Vickers indentation.

2.4. Calculation model of ZrO_2–Nb interface

The theoretical calculations have been performed with the ab initio SIESTA code [34] based on the density functional theory (DFT) [35], using norm-conserving pseudopotentials [36] and the generalized gradient approximation (GGA) with the Perdew, Burke and Ernzerhof (PBE) scheme for the exchange and correlation term [37]. A linear combination of strictly localized numerical atomic orbitals has been used as a basis set, allowing arbitrary angular momenta, multiple-zeta and polarized orbitals. The valence states for Nb and Zr were described by double-zeta (DZ) s- and d-shells together with a single-zeta (SZ) p-shell obtained after polarizing the s-shell. For oxygen, DZ s- and p-shells plus a SZ polarized d-shell were employed [38]. The ZrO_2–Nb interfaces have been modeled within the supercell approach with periodic boundary conditions adhering a ZrO_2 slab periodic in two dimensions (2D) on top of a Nb 2D slab. Both Nb and ZrO_2 slabs are symmetric and there is not vacuum region, thus two equivalent interfaces are present per supercell. This choice ensures zero net dipole moment and hence any unphysical dipole–dipole interactions between neighboring supercells is avoided. The equilibrium structures were obtained self-consistently after relaxation of both unit cell and atomic positions of the slab in the three directions. The final forces were always less than 0.10 eV $Å^{-1}$. The supercell Brillouin zones (BZ) were sampled using a Monkhorst-Pack ($N \times M \times 1$) K-supercells. The K-grid cutoff was larger than 10.5 Å for all the interfaces, which corresponds to $N \times M$ values ranging between 36 and 8 depending on the size of the interface 2D unit cell. Details of the computational conditions can be found elsewhere [20].

The calculated interfaces are characterized by the surface normals of the ceramic and metal slabs and the aligned crystallographic axes in the 2D interface planes. We have considered interfaces constituted by the low index surface orientations of the ZrO_2 and body-centered cubic (bcc) Nb slabs. The selection of the relative alignment of the c-ZrO_2 and Nb 2D crystallographic orientations has been based on geometrical considerations. The selected alignments were among those which present the best overall matching between the constituents surfaces and have the smallest 2D interface unit cells. Generally the ZrO_2 and Nb 2D cells are not completely commensurated and the lattice misfit was assigned to the metal, thus inducing a small in-plane strain at the Nb slab. However, after relaxation the strain is usually distributed between both the ZrO_2

and Nb slabs. The relative positions of the metal and oxide atoms at the interface are those which maximize the number of metal–ceramic bonds. Due to the reduced symmetry the 2D interface unit cells may contain more than one bulk 2D unit. The largest unit cell corresponds to the interface formed by the out-of-plane orientations $ZrO_{2(110)}$–$Nb_{(110)}$, whose 2D cell includes 8 and 18 ZrO_2 and Nb 2D units, respectively. The number of layers depends on the interface and ranges from 19 for the $ZrO_{2(100)}$–$Nb_{(110)}$ to 6 for the $ZrO_{2(110)}$–$Nb_{(110)}$ interface. In all cases bulk-like behavior is retrieved at the central layers of each slab.

3. Results and discussion

3.1. Flaky niobium powders

The ball-milled Nb powder can be textured by the milling process. This texture of the deformed metal particles is revealed by XRD (Fig. 1B). A strong preference for the deformed crystallites to have their (200) reflection parallel to the specimen surface occurred. A strong preference for the {100} type of lattice planes to be parallel to the surface was reported for cold-rolled polycrystalline bcc metals [39]. Ball-milling and cold-rolling imply that the material is flattened in between compressing surfaces; that is, the balls in the ball-milling equipment used here and both rolls in rolling apparatus. The texture can be explained as follows. The most particles that deformed were flattened into flakes, which, after being suspended in acetone (in the procedure for specimen preparation for XRD analysis), position on to the Si substrate with strong tendency for their flat sides to be parallel to the surface of the Si substrate. On the other hand, the measurements of the Nb powders showed that the XRD lines become substantially broadened upon ball-milling (Fig. 1B). This broadening can be ascribed to the introduction of lattice microstrain.

3.2. Microstructure

An optical micrograph of ZrO_2–Nb composite is shown in Fig. 2. In this micrograph the darker and bright phases are zirconia and niobium grains, respectively. The niobium particles are uniformly dispersed in the matrix and no porosity is observed. Thin flakes (each flake is probably a single deformed original particle) are oriented normal to the hot-press direction.

A high-resolution transmission electron micrograph appears in Fig. 3. This micrograph shows a direct contact between both grains at the interfaces without any additional phases. This accords with thermodynamical data [40]. Only a solid solution of Nb_2O_5 in ZrO_2 can take place [27] but the formation of an interphase region has not been observed. On the other hand, it may well be that the oxygen is dissolved and distributed statistically in the niobium [41]. However, no new suboxide should be observable. The interface is rough and the ZrO_2 that is in contact with the Nb seems to have a high defect density. The niobium

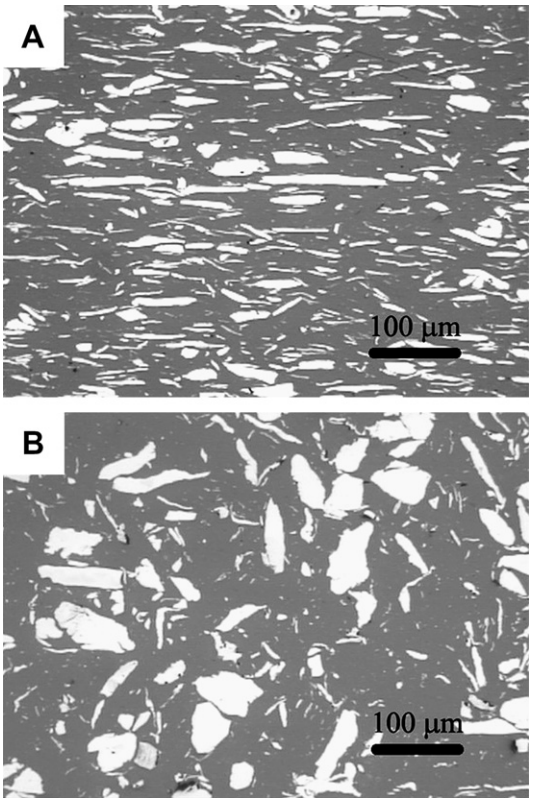

Fig. 2. Optical micrograph of microstructures in zirconia–Nb composite: (A) normal and (B) parallel to hot-press direction. Darker phase is zirconia and lighter phase is Nb.

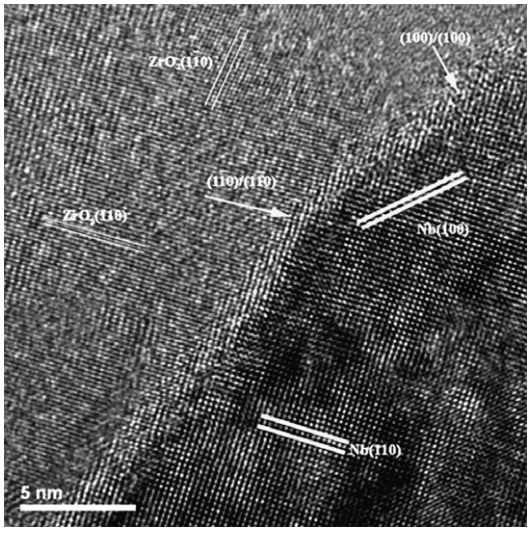

Fig. 3. HRTEM image of the Nb–ZrO_2 interface.

region displays the crystallographic planes (110) and (1$\bar{1}$0) (right and lower corner of Fig. 3). This niobium orientation implies that the planes (001) will be perpendicular to the plane of the sample. Zirconia area seems to have some twinning. However, (220) planes are clearly visible and parallel to the corresponding (110) of niobium. In the right upper region, (2$\bar{2}$0) planes of zirconia can be

distinguished. The interface between zirconia and niobium cannot be defined as a sharp line. Instead it seems to present a polygonal shape. In Fig. 3, the interface at the upper region appears to be parallel to the (100) planes of both niobium and zirconia, while in the central region, a (110)–(1$\bar{1}$0) interface seems to appear. However, in this region several changes of direction of 135° can be observed, corresponding to a change from (110)–(1$\bar{1}$0) to (100)–(100) interfaces. Moreover, the Nb–ZrO_2 interfaces were found to be partially faceted along the (110) planes of Nb grains. These results show that the (110) Nb interface is atomically incoherent and suggest that atomic faceting is the dominant factor in determining the (110) interface plane rather than atomic matching at the interface. These facets at ceramic–metal interface are observed in other systems like Al_2O_3–Nb [42].

3.3. Ab initio calculations

A schematic representation of the 2D primitive cells for the ZrO_2(100)–Nb(100) and $ZrO_{2(110)}$–$Nb_{(110)}$ interfaces are shown in Fig. 4. For the oxide polar surfaces (100) and (111), where both Zr and oxygen terminations are possible, we restrict the analysis to the O-ended case since in general O–metal ionic bonds are stronger than metal–metal bonds [25,43]. The Nb surface orientations considered are the (100), which as revealed by XRD is the majority surface of the deformed metal particles, and the (110), which corresponds to the highest close-packed planes in a bcc crystal structure.

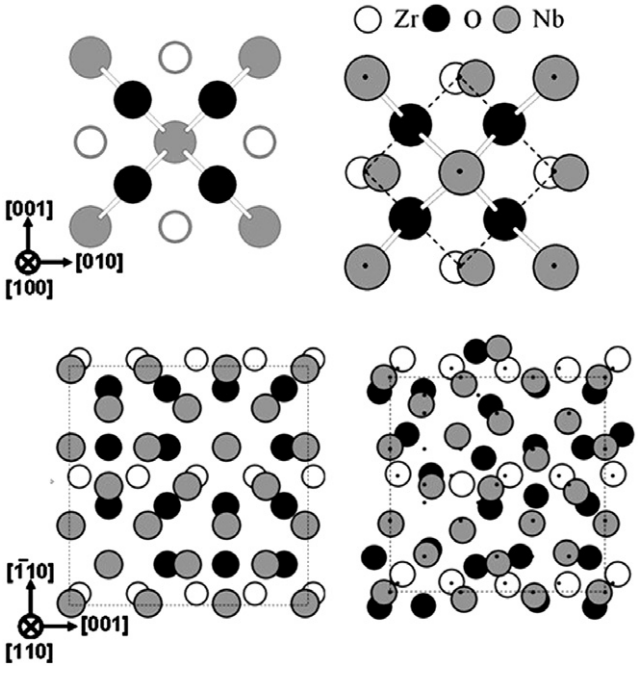

Fig. 4. Top view of the $ZrO_{2(100)}$–$Nb_{(100)}$ (top) and $ZrO_{2(110)}$–$Nb_{(110)}$ (bottom) supercells used to simulate the corresponding interfaces. Only the two atomic planes forming the interface, one for Nb and one for the ZrO_2, are shown. The supercell unit cell is indicated by dashed lines and the crystallographic directions refer to the ZrO_2 lattice. Left and right panels represent the atomic positions of the unrelaxed and relaxed interface structures, respectively.

In Table 1, the work of separation (W_{sep}) of the interfaces is given. The W_{sep} is defined as the difference in the total energy of the ensemble ZrO_2–Nb structure and of the isolated relaxed metal and zirconia systems. As seen in Table 1, there is a large dispersion of the W_{sep} values, which differ by more than an order of magnitude. For a fixed Nb surface the W_{sep} is dependent on the ZrO_2 orientation. The interfaces formed by polar surfaces present the largest values. Because formation of polar surfaces requires the breaking of strong anion–cation ionic bonds, the new bonds formed with the metal at the interface stabilize the highly reactive polar oxide surfaces, which results in strongly adhered interfaces [20].

The fact that the $ZrO_{2(100)}$–$Nb_{(100)}$ interface, with the largest W_{sep}, is observed in the HRTEM micrograph, guarantees the presence of strongly bonded interfaces in the ZrO_2–Nb composite. Furthermore, as explained above, the experimentally found $ZrO_{2(110)}$–$Nb_{(110)}$ interface shows some faceting to accommodate the lattice misfit and thus there are strongly bonded $ZrO_{2(100)}$ and $Nb_{(100)}$ planes between the moderately bonded $ZrO_{2(110)}$ and $Nb_{(110)}$ surfaces. Therefore, the present results support the appearance in the composite of both moderate and strongly bonded areas at the interface between the metal and the ZrO_2. Besides, the $ZrO_{2(110)}$–$Nb_{(110)}$ is thermodynamically the most stable of all the calculated interfaces, which explains its presence in the composite, despite the preference of the deformed Nb particles to have (100) surfaces.

In almost all the calculated interfaces there are several Nb–O strong bonds, as can be inferred from Table 1, where the shortest O–Nb bond length for the different interfaces is presented. In all cases the equilibrium O–Nb distances is smaller than the sum of the Nb and oxygen atomic radii, indicating the existence of a bond between the two atoms. Short O–Nb bonds are present not only in the $ZrO_{2(100)}$–$Nb_{(100)}$ interface, which has the largest W_{sep}, but also in the $ZrO_{2(110)}$–$Nb_{(110)}$, with a moderate W_{sep} value. Therefore, the W_{sep} differences arise from the number of strong O–Nb bonds per unit area. There are cases where the relative distribution of Nb and ceramic atoms is such that leads to a very small, almost null, coordination of O–Nb pairs, and consequently to low W_{sep}. Then, the correlation between W_{sep} and bond strength is intricate partly due to the coexistence of strong and weak bonds at the interface. The bonding is ionic and there is certain charge transfer

Table 1
Work of separation (in J m^{-2}) and interface Nb–O and Nb–Zr distances in Å for the different interfaces

ZrO_2–Nb interface	W_{sep}	d_{Nb-O}	d_{Nb-Zr}
(100)–(100)	9.07	2.07	
(111)–(100)	1.84	2.23	
(110)–(100)	0.41	2.39	3.32
(100)–(110)	6.00	2.12	
(110)–(110)	2.20	2.06	2.87

Please cite this article in press as: Bartolomé JF et al., Influence of ceramic–metal interface adhesion on crack ..., Acta Mater (2008), doi:10.1016/j.actamat.2008.03.021

from the Nb to the oxygen. The ionic character of the interface bonds is clearly appreciated in Fig. 5, which represents the charge density difference (CDD) plot of the $ZrO_{2(100)}$–$Nb_{(100)}$ corresponding to a cross-section containing the interface atoms along the [0 1 0] and [0 0 1] directions. It shows the distribution of the electronic charge due to the interface bonding. Fig. 5 emphasizes the ionic character of the bonds. The Nb atoms show highly localized charge depletion. In contrast the oxygen atom is subjected to minor modifications with respect to bulk zirconia.

3.4. Mechanical properties

The bending strengths, Young's modulus and hardness for the studied specimens are given in Table 2. Taking into account the *R*-curve and the fracture strength values, simple fracture mechanism estimations indicate that the increase in the size of the critical defect in the 3Y-TZP–Nb composites is compensated by a rise in their fracture toughness. Consequently, fracture strength distributions in 3Y-TZP–Nb composites are similar to those in the monolithic 3Y-TZP. *R*-curve behavior of the ZrO_2–Nb composite is shown in Fig. 6 and clearly illustrates the significantly higher fracture resistance of the ceramic–metal composites compared to monolithic ZrO_2. Rising *R*-curve was obtained with a maximum crack-growth resistance almost twice as high as the initial value. Cracking initiated in the ZrO_2–Nb composite at ~8 MPa $m^{1/2}$, and involved stable crack advanced at progressively higher stress intensities exceeding 15 MPa $m^{1/2}$ due to crack bridging by intact Nb lamellar particles in the crack wake; in contrast, the monolithic ZrO_2 failed catastrophically at K_{IC} values of 6.

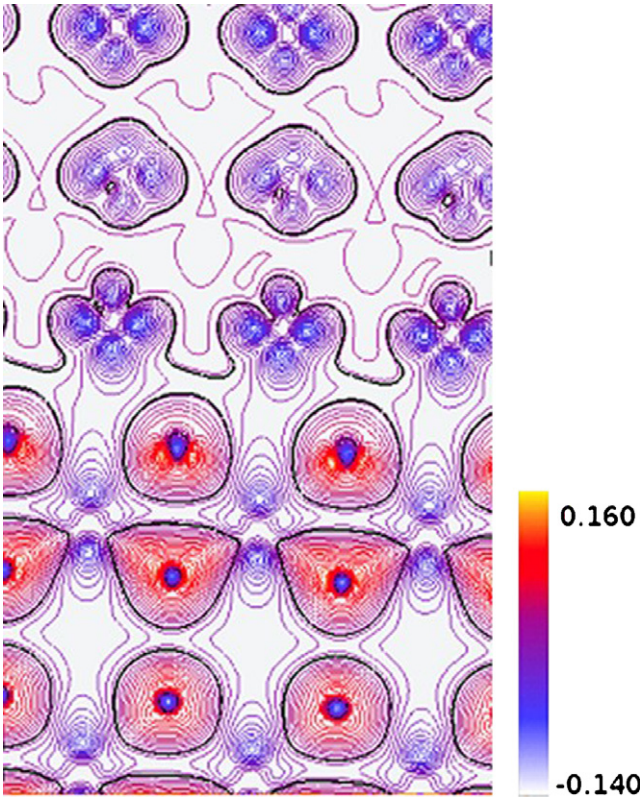

Fig. 5. Spatial distribution of the charge density (CD) difference (total CD minus superposition of atomic CDs) for the $ZrO_{2(100)}$–$Nb_{(100)}$ interface along a plane containing the O–Nb bonds and the directions [0 1 0] and [0 0 1]. The top half represents the Nb slab, the bottom half ZrO_2. Contour lines are taken in steps of 2.2×10^{-3} electrons and the zero level has been marked with a thicker line.

Table 2
Bending strength (σ_f), Young's modulus (E) and mean Vicker's hardness (H_V) of zirconia and zirconia–Nb composites

Material	σ_f (MPa)	E (GPa)	H_V (GPA)
3Y-TZP	800 ± 15	180 ± 5	10.5 ± 0.6
3Y-TZP–Nb	800 ± 10	140 ± 6	6.8 ± 0.7

3.5. Crack–particle interactions

Microstructure–crack interactions were investigated for cracks introduced on the polished surfaces by a Vickers indenter at a load of 490 N (Fig. 7). As can be observed, the major toughening mechanism is the plastic deformation of niobium particles that have been partially debonded. Furthermore, fractographic studies of the materials showed clear evidence of bridging and plastically deformed niobium lamellar particles and matrix–reinforcement interfacial decohesion (Fig. 8). The niobium particles failed in a number of ways: those failing by complete or partial plastic deformation (necking, internal void growth, partial plastic deformation, etc.), those that debonded and pull-out, which contributes very little energy dissipation (deflection), and those that failed by brittle fracture. The proportion of particles failing by each mechanism was determined statis-

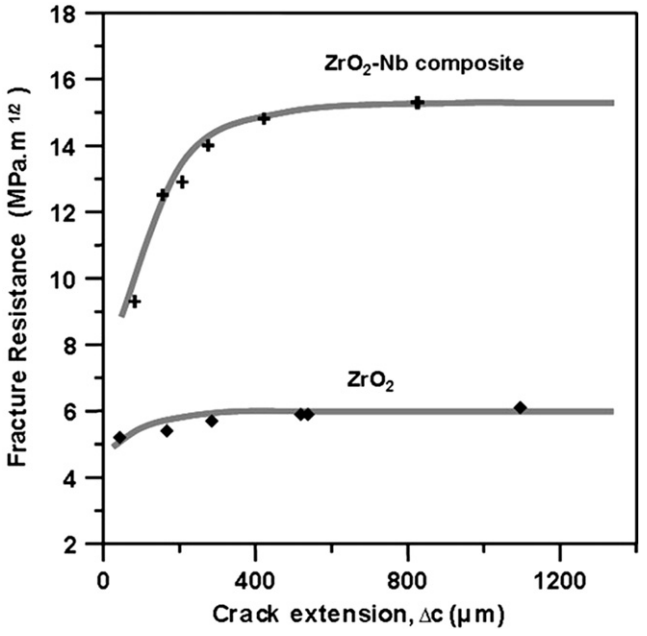

Fig. 6. Comparison of the *R*-curves measured in 3Y-TZP and 3Y-TZP–Nb composites.

Please cite this article in press as: Bartolomé JF et al., Influence of ceramic–metal interface adhesion on crack ..., Acta Mater (2008), doi:10.1016/j.actamat.2008.03.021

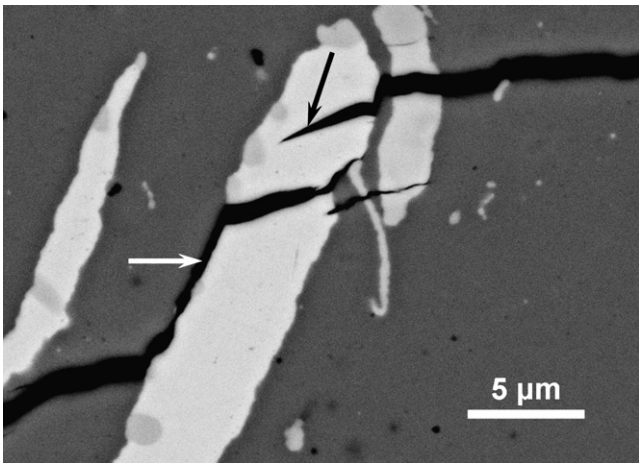

Fig. 7. SEM micrographs showing a indentation crack of 3Y-TZP–Nb composite. White arrow shows the debonding and black arrow shows the plastic deformation.

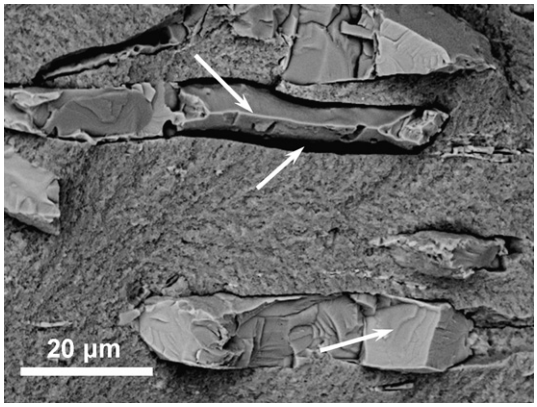

Fig. 8. Fracture surface for cracks extending at the ZrO_2–Nb interface. Upper arrow shows the plastic deformation of a niobium grain. Middle arrow shows the decohesion between the matrix and the niobium particle. Lower arrow shows a brittle cleavage fracture.

tically by SEM examinations of a large number of particles (~100) on the fracture surface. Over 60% of particles were found to fail with some degree of deformation, while about 20% failed in a brittle manner. Among the Nb grains observed in the fracture surface, 20% of the grains were related with pull-out process. Present observation suggests that the dominant toughening mechanism operating in the present ZrO_2–Nb composites is crack bridging, which was strictly limited to elongated grains. This restriction can be explained as follows. At the moment when the crack tip is just behind the toughening Nb grain, this grain is stressed by bending. Because thick grains are less flexible than thin ones, rounded Nb grains may not act as bridge and fail during the period of bending, as observed in Fig. 8. This figure also shows that grains with high aspect ratio are effective in creating crack deflection.

From physical considerations, it is clear that a certain amount of ductility of the reinforcement is needed for any significant improvement in the toughness of brittle matrix composites. It has also been recognized that ductility of the reinforcing phase alone is not sufficient for achieving an improvement in the fracture toughness; equally as important is the matrix–reinforcement interfacial strength. For example, if the interface is very strong, a high degree of constraint can lead to a triaxial state of stress, resulting in a brittle failure of the ductile reinforcement [44]. Consequently, there would not be a significant increase in the composite toughness under these circumstances. Conversely, for very low reinforcement–matrix interface strength, the reinforcement would readily debond and there would be no crack surface bridging action, again resulting in a limited improvement in the toughness [45]. Additionally, a significant improvement in the fracture toughness would be expected if a partial interfacial debonding (decohesion) can remove the geometrical constraints and allow the reinforcement to neck, while the remaining interface area in contact with the matrix (because of a combination of the interface bonding strength and mechanical interlock) allows an effective load transfer to the reinforcement. The metal particles in the matrix remain elastic until a crack approaches. As the crack passes by, the particle surface is subjected to plastic deformation, but the particle itself remains intact by bridging the material even after the crack bypasses the particle. Subsequently, stretching of the metal occurs by plastic flow, ultimately resulting in the total failure of the particle. Then the extensive plastic deformation of the bridging particles before fracture contributes to a substantial toughening.

3.6. Particle–matrix interface properties

The niobium–ceramic matrix interface in the present instance clearly shows evidence of partial decohesion along the fracture surface with associated flaky particles necking and ductile fracture. This suggests that the interface of the composite fabricated by this processing technique possesses optimal interface properties. The brittle cleavage fracture modes observed in the vicinity of regions without debonding in Fig. 8 are attributed to the effects of the high stress triaxiality induced in these regions. The debonding at the Nb–matrix interfaces can also be considered as an evidence of toughness by crack-tip blunting [46].

From XRD investigations alone it can be concluded that the {100} planes of the Nb lattice relative to the interface are the most probable interfacial bond planes. As explained above, the results of the calculations indicate that the $ZrO_{2(100)}$–$Nb_{(100)}$ interfaces posses separations works of 9.07 J m^{-2}. As an example, the separation work determined using $Nb_{(111)}$ and $Al_2O_{3(0001)}$, a model system with good adherence, are typically 9.8 J m^{-2} [47]. Conversely, the $ZrO_{2(111)}$–$Nb_{(100)}$ and $ZrO_{2(110)}$–$Nb_{(100)}$ interfaces present separation works of 1.84 J m^{-2} and 0.41 J m^{-2}, respectively. The work of separation (W_{sep}) is defined as the reversible work needed to separate the interface into two free surfaces whereby plastic and diffusional

Please cite this article in press as: Bartolomé JF et al., Influence of ceramic–metal interface adhesion on crack ..., Acta Mater (2008), doi:10.1016/j.actamat.2008.03.021

processes are suppressed. W_{sep} is a fundamental quantity which characterizes the strength of the metal–ceramic interface. The most stable structures against cleavage of the interface are those with the largest value of the work of separation [17]. Therefore, this combination of weak and strong interfaces made possible both debonding and plastic deformation of the Nb particles. While boundaries with the moderate interface strength are essential for toughening via bridging in ceramic–metal composites, it appears that the optimal window for boundary strength may be small. Indeed, if boundaries are weaker than optimal, the *R*-curves rise less steeply and the crack growth resistance plateau toughness would be lower. It is also obvious that too large boundary strength leads to transgranular fracture and no bridging mechanism. The large differences in plateau toughness between the present work (16 MPa $m^{1/2}$) and the previous one (12 MPa $m^{1/2}$) with the same composition but with Nb particles in a random distribution [27], reflects a major role of the interfacial bonding. In the present work, the larger metallic particles are preferentially oriented due to the effect of the applied pressure during hot-pressing. Much less plastic deformation of Nb particles is observed in the fracture surface of the isostatic press composites with the random distribution of the metal particles, whereas for hot-pressed composites plastic deformation is substantial. These results suggest that increasing the aspect ratio of the distributed Nb reinforcement phase with optimal interfacial strength is a critical factor for the successful development of tougher ZrO_2–Nb structural composites.

Hence the correlation between the structure and properties of the interface, at the atomic level, and the mechanical properties of the materials are contemplated as a necessary requirement to design ceramic–metal composites with an optimum crack growth resistance. Providing an understanding of how local changes at the atomic scale in the oxide–metal bonding modify the macroscopic materials properties, can become in the new future a critical tool for design and tailor new ceramic–metal composites. In this regard we consider that this multiscale relationship is an important topic for future research.

4. Conclusions

From the present study the following conclusions can be drawn:

- Correlations at atomic level have been established between the interface adhesion and the crack growth resistance of 3Y-TZP–Nb composites with lamellar flaky-shape metal particles textured in (100) orientation.
- The work of separation by ab initio calculations of 3Y-TZP–Nb composites were found to be for $ZrO_{2(100)}$–$Nb_{(100)}$, $ZrO_{2(111)}$–$Nb_{(100)}$, $ZrO_{2(110)}$–$Nb_{(100)}$, $ZrO_{2(100)}$–$Nb_{(110)}$ and $ZrO_{2(110)}$–$Nb_{(110)}$ interfaces 9.07, 1.84, 0.41, 6.00 and 2.20 J m^{-2}, respectively. These values justify the observed bridging mechanism in the ceramic–metal composites.
- The *R*-curve showed that the toughness increased higher than 16 MPa $m^{1/2}$ when the crack was longer than 500 μm. The resistance curve behavior is associated with the crack–ductile Nb flaky particle interactions.

Acknowledgements

This work was supported by EU under project reference FP6-515784-2, by the Spanish Ministry of Science and Education under Projects Nos. MAT2006-10249-C02-01 and MAT2006-5122 and by the "Dirección General de Universidades e Investigación de la Consejería de Educación y Ciencia de la Comunidad de Madrid" and CSIC under Project reference 200660M042. J.F.B. has been supported by Ministry of Science and Technology and CSIC under the "Ramón y Cajal" Program co-financed by European Social Fund. The authors also thank A.P. Tomsia and E. Saiz from the Lawrence Berkeley National Laboratory, for samples machining.

References

[1] Krstic VD. Philos Mag 1993;48:695.
[2] Bartolome JF, Diaz M, Moya JS. J Am Ceram Soc 2002;73:2778.
[3] López-Esteban S, Bartolomé JF, Moya JS, Tanimoto T. J Mater Res 2002;17:1592.
[4] Flinn BD, Rühle M, Evans AG. Acta Metall Mater 1989;37:3001.
[5] Sigl LS, Mataga PA, Dalgleish BJ, McMeeking RM, Evans AG. Acta Metall Mater 1988;36:945.
[6] Zimmermann A, Hoffman M, Emmel T, Gross D, Rödel J. Acta Mater 2001;49:3177.
[7] Sbaizero O, Pezzotti G, Nishida T. Acta Mater 1998;46:681.
[8] Ashby MF, Blunt FJ, Bannister M. Acta Metall 1989;37:1847.
[9] Budiasky B, Amagino JC, Evans AG. J Mech Phys Solids 1988;36:167.
[10] Bannister MK, Ashby FM. Acta Metall Mater 1991;39:2575.
[11] Marshall DB, Morris WL, Cox BN, Dadkhah MS. J Am Ceram Soc 1990;73:2938.
[12] Bannister MK, Shercliff HR, Bao G, Zoc F, Ashby MF. Acta Metall 1992;40:1531.
[13] Ikuhara Y, Pirouz P. Microsc Res Techniq 1998;40:206.
[14] Ernst F. Mater Sci Eng A 1995;R14:97.
[15] Rühle M. J Eur Ceram Soc 1996;16:353.
[16] Wagner Th, Lorenz M, Rühle M. J Mater Res 1996;11:1255.
[17] Finnis MW. J Phys Condens Mat 1996;8:5811. Q1
[18] Sinnott SB, Dickey EC. Mater Sci Eng A 2003;R43:1.
[19] Munoz MC, Gallego S, Beltran JI, Cerda J. Surf Sci Rep 2006;61:303.
[20] Beltrán JI, Gallego S, Cerdá J, Moya JS, Muñoz MC. J Phys Chem B 2004;108:15439.
[21] Pecharroman C, Beltran JI, Esteban-Betegon F, Lopez-Esteban S, Bartolome JF, Muñoz MC, et al. Z Metallkd 2005;96:507.
[22] Zhang W, Smith JR, Evans AG. Acta Mater 2002;50:3803.
[23] Hashibon A, Elsässer Ch, Rühle M. Acta Mater 2007;55:1657.
[24] Hashibon A, Elsässer Ch, Rühle M. Acta Mater 2005;53:5323.
[25] Beltrán JI, Gallego S, Cerdá J, Moya JS, Muñoz MC. Phys Rev B 2003;68:075401.
[26] Beltrán JI, Gallego S, Cerdá J, Muñoz MC. J Eur Ceram Soc 2003;23:2737.
[27] Bartolomé JF, Gutiérrez-González CF, Pecharromán C, Moya JS. Acta Mater 2007;55:5924.
[28] Raddatz O, Schneider GA, Mackens W, Vob H, Claussen N. J Eur Ceram Soc 2000;20:2261.
[29] Nagendra N, Jayaram VJ. Mater Res 2000;15:1131.

[30] Hsueh Ch-H, Becher PF. J Am Ceram Soc 1995;78:2237.
[31] Fett Th, Munz D, Seidel J, Stech M, Rödel J. J Am Ceram Soc 1996;79:1189.
[32] Hsueh C, Becher PF. J Am Ceram Soc 1988;71:234.
[33] Braun LM, Benninson SJ, Lawn BR. J Am Ceram Soc 1992;75:3049.
[34] <http://www.uam.es/departamentos/ciencias/fismateriac/siesta/>.
[35] Koch W, Holthausen MC. Chemist's guide to density functional theory. Wiley-VCH; 2001.
[36] Hamman DR, Schlüter M, Chiang C. Phys Rev Lett 1979;43:1494.
[37] Perdew JP, Burke K, Ernzerhof M. Phys Rev Lett 1996;77:3865.
[38] Soler JM, Artacho E, Gale JD, García A, Junquera J, Ordejón P, et al. J Phys Condens Mat 2002;14:2745.
[39] Park YB, Lee DN, Gottstein G. Acta Mater 1998;46:3371.
[40] Asundi MK, Garg SP, Mukhopadhyay P, Tiwari GP, Saroja A. J Alloy Phase Diagrams (India) 1986;2:141.
[41] Kobyakov VP, Ponomarev VI. Crystallogr Rep 2002;47:106.
[42] Evans AG, Rühle M. Microstructure and fracture resistance of metal–ceramic interfaces. In: Wolf D, Yip S, editors. Materials interfaces. Atomic-level structure and properties. London: Chapman & Hall; 1992. p. 54.
[43] Li J-G. Mater Chem Phys 1997;47:126.
[44] Hancock JW, Meckenzie AC. J Mech Phys Solids 1976;24:147.
[45] Venkateswara Rao KT, Soboyejo WO, Ritchie RO. Metall Trans A 1992;23:2249.
[46] Chan KS. Metall Trans A 1992;23:183.
[47] Zhang W, Smith JR. Phys Rev B 2000;61:16883.

Please cite this article in press as: Bartolomé JF et al., Influence of ceramic–metal interface adhesion on crack ..., Acta Mater (2008), doi:10.1016/j.actamat.2008.03.021